REDVET - Revista electrónica de Veterinaria - ISSN 1695-7504
Vol 25, No. 2 (2024)
http://www.veterinaria.org
Article Received: 16 September 2024 Revised: 18 October 2024
Accepted: 09 December 2024

Integrated Spectroscopic, DFT, Molecular Docking and In Vitro Evaluation of 2,6-Diaminoanthraquinone: A Promising Lead for Lung Cancer

Hima S[1], M.R. Meera[2*], C.Vijayakumar[3], R. Premkumar[4]

[1]Research scholar (Reg. No.21123232132004), Department of Physics, St. Jude's College, Thoothoor-629 176, Affiliated to Manonmanium Sundaranar University, Abishekapatti, Tirunelveli-627 012, Tamil Nadu, India.
[2*]Department of physics, Sree Ayyappa College for Women, Chunkankadai, Nagarcoil-629003, Tamil Nadu, India.
[3]Department of Physics, St. Jude's College, Thoothoor, Kanyakumari District-629176, Tamil Nadu, India.
[4]Advanced Materials Research Centre, PG and Research Department of Physics, Nadar Mahajana Sangam S. Vellaichamy Nadar College, Nagamalai, Madurai-625019, Tamil Nadu, India.

***Corresponding Author:** Dr. M.R. Meera, Ph. D
Associate Professor and Head, Department of Physics, Sree Ayyappa College for Women, Chunkankadai, Nagercoil 629 003, Tamil Nadu, India. TEL: +91-9443692523, E-mail: meeranairmrm17@gmail.com

Abstract
The compound 2,6-Diaminoanthraquinone (DAAQ) was investigated through experimental (FT-IR, FT-Raman, UV-Vis) and theoretical (DFT, TD-DFT) approaches, along with in vitro cytotoxicity and molecular docking studies. The optimized molecular structure and vibrational frequencies were obtained using the B3LYP/cc-pVTZ basis set. The vibrational assignments were supported by PED analysis, showing good agreement with experimental spectra. UV-Vis analysis confirmed n→π* electronic transitions associated with the amino and carbonyl functionalities. The FMOs revealed a HOMO–LUMO gap of 2.85 eV, indicating charge transfer properties. Mulliken charge distribution and MEP surface confirmed the role of NH_2 groups and carbonyl oxygens in intramolecular charge transfer. Molecular docking revealed strong binding of DAAQ with lung cancer-related proteins, particularly DPP-4, while in vitro cytotoxicity assays demonstrated significant inhibition of A549 lung cancer cell growth compared to HeLa cervical cancer cells. These combined findings suggest that DAAQ is a promising candidate for targeted lung cancer therapy.

Keywords: 2,6-Diaminoanthraquinone; DFT; Vibrational analysis; Cytotoxicity; Molecular Docking; Lung Cancer

1. Introduction

Lung cancer is the leading cause of cancer-related mortality worldwide, accounting for nearly 18% of all cancer deaths, with more than 2.2 million new cases reported annually [1]. It is primarily associated with risk factors such as tobacco smoking, environmental pollutants, and occupational exposure to carcinogens. The disease is characterized by aggressive progression, late-stage detection, and poor survival rates despite advances in chemotherapy, targeted therapy, and immunotherapy [2]. Cervical cancer, on the other hand, ranks among the top four malignancies in women, with an annual incidence of over 600,000 cases and approximately 340,000 deaths worldwide [3]. Persistent infection with high-risk human papillomavirus (HPV) strains, especially HPV-16 and HPV-18, is a major etiological factor for cervical carcinogenesis. However, challenges such as limited access to screening, vaccination programs, and the emergence of resistant phenotypes highlight the need for new, effective therapeutic agents [4].

Quinones, particularly anthraquinones, constitute an important class of naturally occurring and synthetic compounds with significant pharmacological activities. They are well recognized for their redox properties, ability to generate reactive oxygen species (ROS), and capacity to interact with nucleic acids and proteins, rendering them effective in diverse therapeutic applications including antimicrobial, antiviral, anti-inflammatory, and anticancer treatments [5,6]. Structure–activity relationship (SAR) studies have demonstrated that functional substitutions on the anthraquinone core strongly modulate bioactivity. Specifically, amino substitutions have been found to enhance hydrogen bonding interactions, electron-donating capacity, and pharmacokinetic properties, thereby improving cytotoxic potential against cancer cells [7,8].

2,6-Diaminoanthraquinone (DAAQ) is a derivative of anthraquinone characterized by amino substitutions at the 2 and 6 positions of the aromatic ring system. These functional groups significantly influence the molecule's electronic distribution, frontier orbital energies, and capacity for intramolecular charge transfer, which are key determinants of its chemical reactivity and biological activity. Previous studies have reported that aminoanthraquinone derivatives exhibit promising anticancer effects through mechanisms such as DNA intercalation, inhibition of topoisomerases, and modulation of oxidative stress pathways [9,10]. DAAQ, with its enhanced hydrogen bonding capability, is expected to demonstrate selective cytotoxicity and protein-binding potential, making it a suitable scaffold for drug discovery.

REDVET - Revista electrónica de Veterinaria - ISSN 1695-7504
Vol 25, No. 2 (2024)
http://www.veterinaria.org
Article Received: 16 September 2024 Revised: 18 October 2024
Accepted: 09 December 2024

Spectroscopic investigations, particularly FT-IR, FT-Raman, and UV-Vis analyses, provide insights into the vibrational and electronic properties of bioactive molecules. Complementarily, density functional theory (DFT) enables accurate predictions of optimized molecular geometry, vibrational frequencies, frontier molecular orbitals (FMOs), and charge distribution descriptors [11]. Such combined experimental and computational strategies are widely employed to elucidate structure–property relationships of anthraquinone derivatives. Moreover, molecular docking studies help in identifying potential molecular targets and rationalizing observed cytotoxic effects [12].

In this study, we report a comprehensive evaluation of DAAQ using spectroscopic (FT-IR, FT-Raman, UV-Vis), quantum chemical (DFT, TD-DFT), and biological (in vitro cytotoxicity, molecular docking) approaches. The vibrational spectral assignments are supported by potential energy distribution (PED) analysis. The frontier orbital and Mulliken charge analyses reveal electronic descriptors critical to reactivity, while the molecular electrostatic potential (MEP) maps highlight electrophilic and nucleophilic sites within the molecule. To establish the bioactivity of DAAQ, in vitro cytotoxicity assays were conducted against A549 (lung cancer) and HeLa (cervical cancer) cell lines. Furthermore, docking studies with cancer-related protein targets were performed to elucidate the binding interactions and inhibitory potential of DAAQ. The combined findings underscore the promise of DAAQ as a lead molecule in the development of targeted lung cancer therapeutics.

2. Materials and Methods

2.1 Experimental Characterizations

The 2,6-Diaminoanthraquinone (DAAQ) compound, with a purity of 98%, was purchased from Sigma-Aldrich Chemicals Co. (St. Louis, MO, USA) and used without further purification. The Fourier Transform Infrared (FT-IR) spectrum was recorded at room temperature in the range 4000–400 cm^{-1} using a PerkinElmer Spectrum 1 spectrometer with the KBr pellet technique. The spectral resolution was maintained at 1 cm^{-1}. The Fourier Transform Raman (FT-Raman) spectrum was obtained with a Bruker RFS 27 spectrometer equipped with a Nd:YAG laser operating at 1064 nm, with a spectral resolution of 2 cm^{-1}. Both FT-IR and FT-Raman spectra were measured in the region 3500–400 cm^{-1}. The ultraviolet-visible (UV-Vis) absorption spectrum of DAAQ was recorded using a Shimadzu UV-3600 UV-Vis-NIR spectrophotometer in the wavelength range of 200–600 nm. Ethanol was used as the solvent medium for sample preparation. The anticancer potential of DAAQ was evaluated using the 3-(4,5-dimethylthiazol-2-yl)-2,5-diphenyltetrazolium bromide (MTT) assay. The cytotoxic activity was studied against two human cancer cell lines: A549 (human lung carcinoma) and HeLa (human cervical carcinoma). Cells were cultured in Dulbecco's Modified Eagle Medium (DMEM) supplemented with 10% fetal bovine serum (FBS) and 1% penicillin-streptomycin. Various concentrations of DAAQ (0–360 µg/mL) were applied for 24 h. After incubation, 20 µL of MTT solution (5 mg/mL) was added to each well and further incubated for 4 h. The formazan crystals formed were solubilized with dimethyl sulfoxide (DMSO), and the absorbance was measured at 570 nm using a microplate reader. The IC_{50} values were determined from dose–response curves.

2.2 Computational Details

The molecular geometry of DAAQ was optimized using Density Functional Theory (DFT) at the B3LYP/cc-pVTZ level, as implemented in the Gaussian 09W software package [13]. The optimized structure was confirmed as a true minimum by frequency calculations, which yielded no imaginary frequencies. Vibrational frequencies were calculated and assigned with the aid of Potential Energy Distribution (PED) analysis performed using the VEDA 4.0 program [14]. To account for anharmonic effects, scaling factors of 0.9577 (stretching modes) and 0.9968 (bending modes) were applied. The electronic absorption spectra were simulated using Time-Dependent Density Functional Theory (TD-DFT) at the B3LYP/cc-pVTZ level, employing the Polarizable Continuum Model (PCM) with ethanol as the solvent. Theoretical spectra, including UV-Vis absorption maxima, oscillator strengths, and electronic transitions, were analyzed and compared with experimental results. The frontier molecular orbitals (HOMO and LUMO), Mulliken atomic charge distribution, and Molecular Electrostatic Potential (MEP) surface were visualized using GaussView 05 software [15]. Global reactivity descriptors such as ionization energy, electron affinity, chemical hardness, softness, electronegativity, and electrophilicity index were derived using Koopmans' theorem.

2.3 Molecular Docking Studies

Molecular docking simulations were performed to predict the binding interactions of DAAQ with cancer-related protein targets. The AutoDock 4.0.1 software package was employed [16]. Protein structures were retrieved from the Protein Data Bank (PDB). For lung cancer studies, the Dipeptidyl Peptidase-4 (DPP-4, PDB ID: 2ONC) was selected as a target protein [17]. For cervical cancer, the p38α Mitogen-activated protein kinase (MAPK14, PDB ID: 3FMK) was chosen [18]. The protein structures were prepared by removing water molecules and co-crystallized ligands, followed by the addition of polar hydrogens and Kollman charges. The ligand (DAAQ) structure was optimized at the DFT/B3LYP/cc-pVTZ level and converted into the PDBQT format. Docking parameters were set with a grid box encompassing the active sites of the proteins. The Lamarckian Genetic Algorithm (LGA) was used with 100 runs, a population size of 150,

REDVET - Revista electrónica de Veterinaria - ISSN 1695-7504
Vol 25, No. 2 (2024)
http://www.veterinaria.org
Article Received: 16 September 2024 Revised: 18 October 2024
Accepted: 09 December 2024

and a maximum of 2.5×10^6 energy evaluations. The best binding poses were selected based on the lowest binding energy and interaction profiles. Docking visualizations were generated using PyMOL and Discovery Studio Visualizer.

2.4 In Vitro Cytotoxicity Studies

The MTT assay was used to assess the cytotoxicity of DAAQ against A549 and HeLa cells, as described in section 2.1. Cell viability was expressed as a percentage of control (untreated) cells. The IC_{50} values were calculated using nonlinear regression analysis. Morphological changes in treated cells were observed under an inverted phase-contrast microscope to confirm cytotoxic effects such as cell shrinkage, membrane blebbing, and detachment, indicative of apoptotic cell death.

3. Results and Discussion

3.1 Molecular geometry and symmetry

The DAAQ molecular structure was optimized at the DFT/B3LYP/cc-pVTZ level. The single point electronic energy of the optimized geometry was calculated as −799.29 a.u. (B3LYP/cc-pVTZ). The optimized geometry (Fig. 1) belongs to the C_1 point group and the calculated atomic coordinates give a planar, fully conjugated anthraquinone framework bearing amino substituents at C2 and C6 [19].

A selection of the most relevant bond lengths, bond angles and dihedral angles is given in Table 1. Inspection of the computed bond distances shows that the aromatic C–C bonds of the anthraquinone core lie in the narrow interval 1.387–1.417 Å (C3–C4 = 1.3871 Å, C2–C3 = 1.4169 Å, C1–C2 = 1.4107 Å and C15–C17 = 1.4159 Å). These values are characteristic of delocalized sp^2 carbon–carbon frameworks and indicate extensive π-conjugation across the three fused rings. The near-uniform C–C bond lengths confirm that the π-electron density is highly delocalized over the aromatic skeleton [20].

The carbonyl groups retain strong double-bond character: the computed C9–O11 and C10–O12 bond lengths are 1.2579 Å, consistent with typical C=O distances in quinone units. The C9–C15 and C10–C16 bonds (1.4920 Å) and the adjacent C9–C18/C10–C17 distances (1.4686 Å / 1.4686 Å) reflect the altered bond order around the carbonyl-bearing carbons due to electron-withdrawing character of the C=O groups and conjugation with the aromatic rings.

The amino substituents show C–N distances C2–N13 = 1.3760 Å and C6–N14 = 1.3760 Å, substantially shorter than a typical C–N single bond and indicative of partial double-bond character resulting from resonance conjugation ($–NH_2$ → aromatic π-system). The N–H bond lengths (N13–H25 = 1.0057 Å, N13–H26 = 1.0055 Å; N14–H27 = 1.0055 Å, N14–H28 = 1.0057 Å) are typical for covalent N–H bonds and confirm the presence of intact amino functionalities in the optimized gas-phase geometry.

Analysis of bond angles shows values typical of sp^2 hybridization throughout the aromatic scaffold. Angles in the ring systems are close to 120° (for example C2–C1–C15 = 120.76°, C3–C2–N13 = 120.77°, C3–C4–C17 = 121.16°), whereas angles centered on carbonyl carbons (O11–C9–C15 =120.54°, O12–C10–C16 =120.54°) reflect trigonal planar geometry at the carbonyl centers. The N-centered angles (C2–N13–H25 =120.89°, H25–N13–H26 =117.95°) indicate that the amino nitrogens are substantially planar, supporting their conjugation with the aromatic π-system rather than adopting a pyramidal geometry.

Selected dihedral angles are either close to 0° or 180° (C15–C1–C2–C3 = 0.00°, C15–C1–C2–N13 = −180.0°, O11–C9–C15–C17 = 180.0°), indicating that the anthraquinone core and the substituents are essentially coplanar. In particular, the near-planarity of the C–N–H moieties with the aromatic rings promotes effective overlap between the lone pair on nitrogen and the π-system of the ring, thereby facilitating intramolecular charge delocalization from the electron-donating amino groups toward the electron-withdrawing carbonyl moieties.

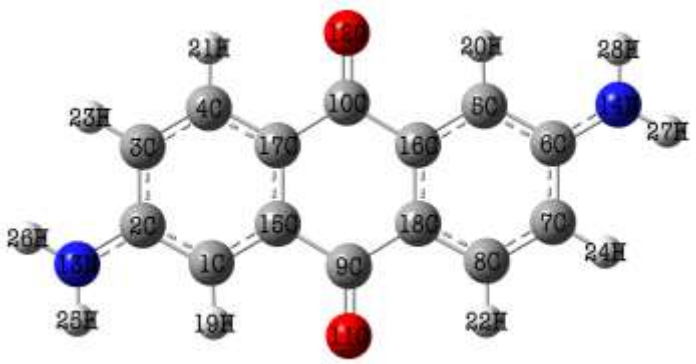

Fig.1. The optimized molecular structure of DAAQ molecule

REDVET - Revista electrónica de Veterinaria - ISSN 1695-7504
Vol 25, No. 2 (2024)
http://www.veterinaria.org
Article Received: 16 September 2024 Revised: 18 October 2024
Accepted: 09 December 2024

Table 1. The optimized structural parameters of the DAAQ molecule calculated by the DFT/B3LYP method with cc-pVTZ basis set.

Bond length	**Value (Å)**	**Bond length**	**Value (Å)**
C1–C2	1.4107	C5–C6	1.4107
C1–C15	1.3924	C5–C16	1.3924
C1–H19	1.0851	C5–H20	1.0851
C2–C3	1.4169	C6–C7	1.4169
C2–N13	1.3760	C6–N14	1.3760
C3–C4	1.3871	C7–C8	1.3871
C3–H23	1.0862	C7–H24	1.0862
C4–C17	1.4067	C8–C18	1.4067
C4–H21	1.0843	C8–H22	1.0843
C9–O11	1.2579	C10–O12	1.2579
C9–C15	1.4920	C10–C16	1.4920
C9–C18	1.4686	C10–C17	1.4686
N13–H25	1.0057	N14–H27	1.0055
N13–H26	1.0055	N14–H28	1.0057
C15–C17	1.4159	C16–C18	1.4159
Bond angle	**Value (°)**	**Bond angle**	**Value (°)**
C2–C1–C15	120.76	C6–C5–C16	120.76
C2–C1–H19	121.02	C6–C5–H20	121.02
C15–C1–H19	118.22	C16–C5–H20	118.22
C1–C2–C3	118.63	C5–C6–C7	118.63
C1–C2–N13	120.60	C5–C6–N14	120.60
C3–C2–N13	120.77	C7–C6–N14	120.77
C2–C3–C4	120.39	C6–C7–C8	120.39
C2–C3–H23	119.45	C6–C7–H24	119.45
C4–C3–H23	120.15	C8–C7–H24	120.15
C3–C4–C17	121.16	C7–C8–C18	121.16
C3–C4–H21	120.77	C7–C8–H22	120.77
C17–C4–H21	118.07	C18–C8–H22	118.07
O11–C9–C15	120.54	O12–C10–C16	120.54
O11–C9–C18	121.82	O12–C10–C17	121.82
C15–C9–C18	117.64	C16–C10–C17	117.64
C2–N13–H25	120.89	C6–N14–H27	121.16
C2–N13–H26	121.16	C6–N14–H28	120.89
H25–N13–H26	117.95	H27–N14–H28	117.95
C1–C15–C9	118.68	C5–C16–C10	118.68
C1–C15–C17	120.46	C5–C16–C18	120.46
C9–C15–C17	120.85	C10–C16–C18	120.85
Dihedral angle	**Value (°)**	**Dihedral angle**	**Value (°)**
C15–C1–C2–C3	0.00	C16–C5–C6–C7	0.00
C15–C1–C2–N13	-180.0	C16–C5–C6–N14	180.0
C19–C1–C2–C3	180.0	C20–C5–C6–C7	180.0
C19–C1–C2–N13	0.00	C20–C5–C6–N14	0.00
C2–C3–C4–C17	0.00	C6–C7–C8–C18	0.00
O11–C9–C15–C1	0.00	O12–C10–C16–C5	0.00
O11–C9–C15–C17	180.0	O12–C10–C16–C18	180.0
C18–C9–C15–C1	-180.0	C17–C10–C16–C5	-180.0
C18–C9–C15–C17	0.00	C17–C10–C16–C18	0.00

3.2 Vibrational Analysis

DAAQ contains 28 atoms and, being non-linear, shows 3N–6 = 78 normal modes, all of A symmetry (C_1 point group). Computed harmonic frequencies were scaled before comparison with experiment, and PED was used to validate mode character. The simulated and observed infrared and Raman spectra of the DAAQ molecule is depicted in Fig. 2 and Fig.3, respectively. The complete set of calculated and scaled frequencies, IR intensities, Raman scattering activities, reduced masses, force constants, and assignments is given in your Table 2.

REDVET - Revista electrónica de Veterinaria - ISSN 1695-7504
Vol 25, No. 2 (2024)
http://www.veterinaria.org
Article Received: 16 September 2024 Revised: 18 October 2024
Accepted: 09 December 2024

3.2.1 Aromatic C–H stretching vibrations

Aromatic ν(C–H) bands appear at 3044–3082 cm^{-1} (scaled) with multiple closely spaced modes at 3044, 3045, 3067–3068, 3081–3082 cm^{-1}, each dominated by C–H stretching character (PED ≈ 96–99%**). IR intensities are generally weak–moderate, while several modes show strong Raman activities, consistent with aromatic stretches being Raman-prominent [21,22].

3.2.2 NH_2 stretching vibrations

The NH_2 symmetric stretches occur near 3465–3466 cm^{-1} and the asymmetric stretches at 3586–3587 cm^{-1} (scaled). These are intense (high IR and very large Raman activities) and exhibit ~96–98% NH_2 stretching character in the PED analysis, confirming the assignments.

3.2.3 C=O stretching and C=C ring coupling

In DAAQ the carbonyl stretch is strongly coupled with the conjugated ring. A prominent mixed ν(C=O)/ν(C=C) band appears at ~1611 cm^{-1} (scaled) with a force constant ≈ 11.08 mDyne $Å^{-1}$, indicating a stiff coordinate. Neighboring bands from ~1528 to 1587 cm^{-1} carry dominant aromatic C–C stretching mixed with in-plane C–H bending and show enhanced Raman activities, mapping the C=O–ring conjugation of the anthraquinone core [23].

3.2.4 Aromatic C–C stretching and in-plane C–H bending

The 1430–1590 cm^{-1} window (scaled) is populated by aromatic C–C stretches mixed with β(C–H) in-plane bends. Intense representatives occur at 1528, 1549, and 1587 cm^{-1}; PED typically attributes ~58–67% to C–C stretching with the remainder from in-plane C–H bending. Several of these modes are Raman-strong due to large polarizability changes.

3.2.5 NH_2 in-plane bending

Two pronounced NH_2 scissoring modes are found at ~1630–1631 cm^{-1} (scaled) with PED ≈ 85% for the NH_2 bend. Although they lie near the C=O/C=C envelope, PED cleanly identifies their scissoring nature.

3.2.6 In-plane C–H bending, C–N stretching, and ring deformation

Between ~1076 and 1350 cm^{-1} (scaled), numerous modes show dominant β(C–H) in-plane bending with notable C–N stretching and ring deformation contributions. This region contains several strong IR bands; a standout occurs near 1282 cm^{-1} with IR intensity ≈ 414.6 Km mol^{-1}, reflecting substantial dipole-moment change. Typical PED values here are ~54–59% β(C–H) with additional C–N and ring components.

3.2.7 Out-of-plane C–H bending and ring deformations

The γ(C–H) out-of-plane and ring-deformation modes cluster at ~828–976 cm^{-1} (scaled). Several modes in this interval carry >60–68% out-of-plane C–H/ring-deformation character by PED, with moderate IR intensities and modest Raman activities—consistent with typical aromatic OOP profiles [22,23].

3.2.8 Ring-breathing modes

Characteristic ring-breathing bands are identified near ~801 cm^{-1} and ~862 cm^{-1} (scaled). The lower-frequency breathing mode is typically Raman-enhanced, while the higher-frequency partner includes additional coupling to ring deformation coordinates, as reflected in the assignments [21].

3.2.9 Low-frequency torsions and skeletal motions

Below ~600 cm^{-1} (scaled), the spectrum is dominated by skeletal torsions, bends, and librations of the anthraquinone core and NH_2 substituents. Very low-frequency modes (≈40–175 cm^{-1}) show external-like torsions and out-of-plane skeletal motions with large PED contributions (>80%), whereas 200–575 cm^{-1} contains mixed ring deformations and bending motions with moderate IR and variable Raman activity.

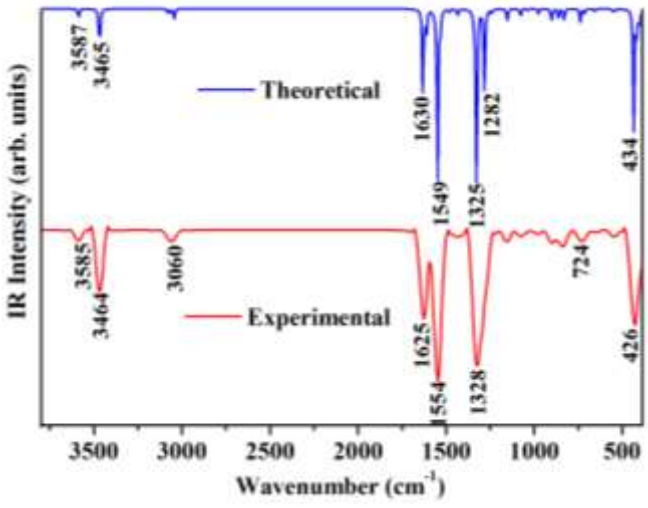

Fig. 2. The theoretical and observed infrared spectra of DAAQ molecule

REDVET - Revista electrónica de Veterinaria - ISSN 1695-7504
Vol 25, No. 2 (2024)
http://www.veterinaria.org
Article Received: 16 September 2024 Revised: 18 October 2024
Accepted: 09 December 2024

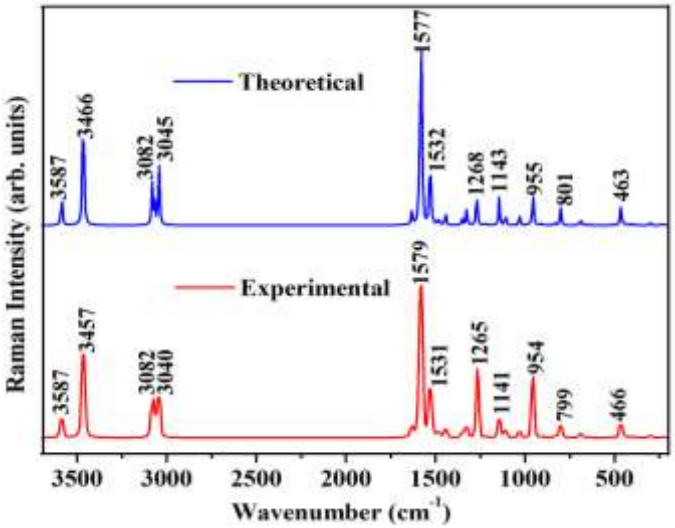

Fig. 3. The simulated and observed Raman spectra of the DAAQ molecule

Table 2. The calculated vibrational frequencies (cm^{-1}), IR intensities (Km mol^{-1}), Raman scattering activity ($Å^4$ amu^{-1}), reduced mass (amu), force constants (mDyne/$Å^{-1}$) and vibrational assignments based on PED calculations for the DAAQ molecule.

S. No.	Observed Wavenumber (cm^{-1})		Wavenumber (cm^{-1})		IR Intensity (Km mol^{-1})	Raman scattering activity ($Å^4$ amu^{-1})	Reduced Mass (amu)	Force Constant (mDyne/ $Å^{-1}$)	Assignment with PED (%)
	FT-IR	FT-Raman	Calculated	Scaled					
1			42	40	10.0080	0.0000	6.7550	0.0073	Torsion / skeletal motion (85%)
2			98	93	0.1232	0.0000	4.5175	0.0259	Skeletal torsion / out-of-plane bend (82%)
3			114	108	0.0000	2.1689	5.7759	0.0448	Skeletal torsion / out-of-plane bend (81%)
4			148	141	0.3238	0.0000	6.4394	0.0841	Skeletal torsion / out-of-plane bend (84%)
5			171	163	4.7266	0.0000	4.7789	0.0824	Skeletal torsion / out-of-plane bend (87%)
6			184	175	0.0000	6.8056	4.8571	0.0971	Skeletal torsion / out-of-plane bend (56%)
7			244	232	0.0000	3.7399	5.4898	0.1932	Skeletal bends / torsion (68%)
8			275	262	15.5414	0.0000	4.5504	0.2033	Skeletal bends / torsion (70%)
9			312	297	0.0000	4.9050	4.8800	0.2805	Skeletal bends / torsion (76%)
10			323	307	0.0000	1.8130	7.3819	0.4559	Skeletal bends / torsion (77%)
11			374	356	19.7657	0.0000	7.0094	0.5785	Skeletal bends / torsion (56%)
12			395	376	0.0000	1.2586	5.1532	0.4745	Skeletal bends / torsion (68%)
13			402	383	7.1053	0.0000	4.0082	0.3828	Skeletal bends / torsion (79%)
14			423	403	0.0000	3.8399	1.0414	0.1098	NH_2 out-of-plane bending (57%)
15			423	403	55.8969	0.0000	1.0426	0.1101	NH_2 out-of-plane bending (53%)
16			438	417	128.0424	0.0000	2.3931	0.2706	C–H out-of-plane bending (42%)
17			449	428	0.0000	0.2396	1.2527	0.1489	Ring deformation (34%)
18	426		456	434	547.3059	0.0000	1.4535	0.1786	Ring deformation (38%)
19			459	437	0.0000	2.7800	4.4003	0.5483	C–H out-of-plane bending /deformations (44%)
20			469	447	0.0000	1.3741	3.2321	0.4206	C–H out-of-plane bending / deformations (43%)
21		466	486	463	0.0000	51.8317	10.4979	1.4621	Ring deformation (37%)
Table 2 (Continued)									
S. No.	**Observed Wavenumber (cm^{-1})**		**Wavenumber (cm^{-1})**		**IR Intensity (Km mol^{-1})**	**Raman scattering activity ($Å^4$ amu^{-1})**	**Reduced Mass (amu)**	**Force Constant (mDyne/ $Å^{-1}$)**	**Assignment with PED (%)**
	FT-IR	**FT-Raman**	**Calculated**	**Scaled**					
22			536	511	0.0000	1.9869	6.3414	1.0745	Ring deformation (36%)
23			571	544	21.2551	0.0000	5.8811	1.1335	Ring deformation (55%)
24			603	574	0.0068	0.0000	3.4058	0.7304	Ring deformation (43%)
25			665	634	0.0000	1.6304	6.6255	1.7309	Ring deformation (50%)

REDVET - Revista electrónica de Veterinaria - ISSN 1695-7504
Vol 25, No. 2 (2024)
http://www.veterinaria.org
Article Received: 16 September 2024 Revised: 18 October 2024
Accepted: 09 December 2024

26			685	653	11.5782	0.0000	6.5768	1.8222	C–H out-of-plane bending / ring deformations (48%)
27			697	664	0.0000	1.1771	3.1992	0.9177	Ring deformation (58%)
28			723	689	0.0000	18.2435	6.8772	2.1197	Ring deformation (50%)
29			745	710	1.8782	0.0000	3.5213	1.1543	C–H out-of-plane bending / ring deformations (46%)
30			750	715	22.3603	0.0000	6.7431	2.2354	C–H out-of-plane bending / ring deformations (58%)
31	724		775	738	56.9002	0.0000	7.3561	2.6093	C–H out-of-plane bending / ring deformations (54%)
32			833	794	0.0000	1.4808	2.7082	1.1092	C–H out-of-plane bending / ring deformations (68%)
33		799	841	801	0.0000	46.4900	5.9785	2.4918	Ring Breathing
34			869	828	61.7596	0.0000	1.5070	0.6714	C–H out-of-plane bending / ring deformations (67%)
35			873	832	0.0000	4.7221	1.8603	0.8365	C–H out-of-plane bending (62%)
36			905	862	42.6161	0.0000	6.8721	3.3211	Ring breathing
37			946	901	60.6867	0.0000	1.5675	0.8268	C–H out-of-plane bending (54%)
38			949	904	0.0000	4.2651	1.6389	0.8709	C–H out-of-plane bending (46%)
39		954	1002	955	0.0000	98.6465	3.5523	2.1026	C–H out-of-plane bending (54%)
40			1020	972	1.1048	0.0000	1.3581	0.8333	C–H out-of-plane bending (65%)

Table 2 (Continued)

S. No.	Observed Wavenumber (cm^{-1})		Wavenumber (cm^{-1})		IR Intensity (Km mol^{-1})	Raman scattering activity ($Å^4$ amu^{-1})	Reduced Mass (amu)	Force Constant (mDyne/ $Å^{-1}$)	Assignment with PED (%)
	FT-IR	FT-Raman	Calculated	Scaled					
41			1021	973	0.0000	2.2253	1.3712	0.8423	C–H out-of-plane bending (65%)
42			1024	976	22.3225	0.0000	2.3103	1.4299	NH_2 in-plane bending / ring deformations (68%)
43			1081	1030	0.0000	24.4045	1.6020	1.1034	NH_2 in-plane bending (67%)
44			1089	1038	5.3441	0.0000	1.5438	1.0794	NH_2 in-plane bending (68%)
45			1129	1076	33.5700	0.0000	3.5463	2.6669	NH_2 in-plane bending (67%)
46			1163	1108	0.0000	32.4218	1.8799	1.4983	In-plane CH bending / C–N stretching / deformation 57%)
47		1141	1199	1143	0.0000	78.1101	1.6443	1.394	In-plane CH bending (58%)
48			1209	1152	61.6813	0.0000	1.4149	1.2203	In-plane CH bending (59%)
49			1278	1218	0.0000	2.9114	1.6271	1.567	In-plane CH bending (55%)
50			1302	1241	17.673	0.0000	1.6396	1.6379	In-plane CH bending / C–N stretching (54%)
51		1265	1331	1268	0.0000	116.7114	3.925	4.0982	In-plane CH bending / C–N stretching /deformation (55%)
52			1345	1282	414.5979	0.0000	2.5628	2.7344	In-plane CH bending / C–N stretching (54%)
53	1328		1390	1325	798.4680	0.0001	4.5144	5.1461	In-plane CH bending / C–N stretching / deformation (55%)
54			1391	1326	0.0017	46.3340	2.3089	2.6322	In-plane CH bending / C–N stretching / deformation (56%)
55			1403	1337	93.0508	0.0000	5.8346	6.7741	In-plane CH bending / C–N stretching / deformation (47%)
56			1416	1350	0.0000	20.0159	7.2673	8.5964	In-plane CH bending / C–N stretching / deformation (55%)

Table 2 (Continued)

S. No.	Observed Wavenumber (cm^{-1})		Wavenumber (cm^{-1})		IR Intensity (Km mol^{-1})	Raman scattering activity ($Å^4$ amu^{-1})	Reduced Mass (amu)	Force Constant (mDyne/ $Å^{-1}$)	Assignment with PED (%)
	FT-IR	FT-Raman	Calculated	Scaled					
57			1502	1432	30.2127	0.0000	3.6476	4.8491	Aromatic C–C stretching and in-plane CH bending (60%)
58			1514	1443	0.0000	41.4973	3.9688	5.3639	Aromatic C–C stretching and in-plane CH bending (58%)
59			1552	1479	10.7848	0.0000	3.5542	5.0445	Aromatic C–C stretching and in-plane CH bending (58%)
60			1555	1482	0.0000	23.6018	3.6147	5.1536	Aromatic C–C stretching and in-plane CH bending (60%)
61			1603	1528	0.0000	283.3827	7.0852	10.7385	Aromatic C–C stretching and in-plane CH bending (60%)
62		1531	1607	1532	87.1233	0.0000	7.0320	10.7071	Aromatic C–C stretching and in-plane CH bending (60%)
63	1554		1625	1549	851.5445	0.0000	7.2399	11.2713	Aromatic C–C stretching and in-

REDVET - Revista electrónica de Veterinaria - ISSN 1695-7504
Vol 25, No. 2 (2024)
http://www.veterinaria.org
Article Received: 16 September 2024 Revised: 18 October 2024
Accepted: 09 December 2024

									plane CH bending (60%)
64		1579	1655	1577	0.0000	514.5747	9.8615	15.9178	Aromatic C–C stretching and in-plane CH bending (67%)
65			1665	1587	0.0000	301.8266	5.8290	9.5263	Aromatic C–C stretching and in-plane CH bending (67%)
66			1690	1611	134.571	0.0000	6.5831	11.0847	C=O / aromatic C=C mixed stretch (65%)
67	1625		1710	1630	420.9655	0.0000	1.1883	2.0482	NH_2 in plane bending (85%)
68			1711	1631	0.0000	43.0333	1.1689	2.016	NH_2 in plane bending (85%)
69			3193	3044	45.4060	0.0000	1.0895	6.5448	Aromatic C–H stretch (97%)
70			3194	3045	0.0000	287.3154	1.0895	6.5451	Aromatic C–H stretch (96%)
71	3060		3217	3067	14.9359	0.0002	1.0905	6.6501	Aromatic C–H stretch (98%)
72			3218	3068	0.0000	109.6255	1.0904	6.6504	Aromatic C–H stretch (96%)

Table 2 (Continued)

	Observed Wavenumber (cm^{-1})		**Wavenumber (cm^{-1})**		**IR Intensity (Km mol^{-1})**	**Raman scattering activity ($Å^4$ amu^{-1})**	**Reduced Mass (amu)**	**Force Constant (mDyne/ $Å^{-1}$)**	**Assignment with PED (%)**
	FT-IR	**FT-Raman**	**Calculated**	**Scaled**					
73			3232	3081	14.8242	0.0006	1.0932	6.7290	Aromatic C–H stretch (97%)
74			3233	3082	0.0000	188.1617	1.0933	6.7303	Aromatic C–H stretch (99%)
75	3464		3635	3465	227.5355	0.0001	1.0450	8.1390	NH_2 symmetric stretch (97%)
76		3457	3636	3466	0.0000	837.2405	1.0451	8.1410	NH_2 symmetric stretch (96%)
77		3587	3762	3586	0.0110	180.9488	1.1035	9.2057	NH_2 asymmetric stretch (98%)
78	3585		3763	3587	48.7997	0.0410	1.1035	9.2058	NH_2 asymmetric stretch (98%)

3.3 UV-Visible analysis

The electronic absorption spectrum of the DAAQ molecule was recorded in ethanol solution and compared with the theoretical results obtained from TD-DFT calculations [24]. The calculated and experimental UV–Vis spectral parameters, together with their assignments, are summarized in Table 3. The experimental and simulated UV-Vis spectrum of the DAAQ molecule is shown in Fig. 4. The TD-DFT calculations predict a major absorption band at 372 nm (3.39 eV) with an oscillator strength of 0.2011, which is attributed to a HOMO → LUMO transition (98%), corresponding to an n → π electronic excitation. Experimentally, this band was observed at 386 nm (3.27 eV), showing a red shift of about 14 nm compared to the calculated value. Such deviation is expected since the theoretical data correspond to isolated molecules, while the experimental measurements were performed in ethanol, where solvation and intermolecular interactions stabilize the excited states.

The close agreement between calculated and observed spectral features indicates that the TD-DFT method with the applied basis set reliably reproduces the electronic transitions of DAAQ. The strong oscillator strength suggests a high probability of electronic excitation, consistent with the intensity of the experimental absorption band. The dominant n → π transition observed in the UV–Vis spectrum of DAAQ reflects the participation of lone-pair electrons in the conjugated system, which plays an essential role in the molecule's photophysical behavior. This transition may contribute significantly to the optical properties and potential applications of DAAQ in photonic and optoelectronic devices.

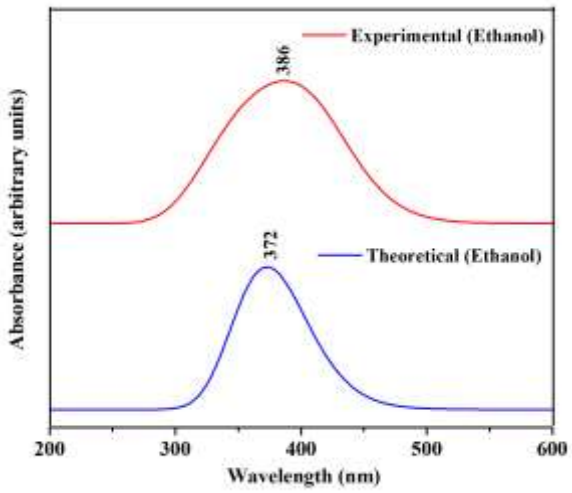

Figure 4. UV-visible spectra of the DAAQ molecule.

REDVET - Revista electrónica de Veterinaria - ISSN 1695-7504
Vol 25, No. 2 (2024)
http://www.veterinaria.org
Article Received: 16 September 2024 Revised: 18 October 2024
Accepted: 09 December 2024

Table 3. The calculated and observed UV-Vis spectral parameters in ethanol solution for DAAQ molecule with its assignments.

Calculated				Observed		Assignment
λ (nm)	E (eV)	F	Orbital contribution	λ (nm)	E (eV)	
372	3.39	0.2011	H→L (98%)	386	3.27	n→π*

3.4 Frontier molecular orbitals (FMOs) analysis

The chemical reactivity and stability of organic molecules can be effectively understood by analyzing their frontier molecular orbitals (FMOs). The highest occupied molecular orbital (HOMO) and the lowest unoccupied molecular orbital (LUMO) are the most significant orbitals that govern electron transfer, optical transitions, and intermolecular interactions. The HOMO represents the electron-donating ability of a molecule, whereas the LUMO corresponds to its electron-accepting capacity [25].

The calculated FMO plots of the DAAQ molecule, shown in Fig. 5, reveal the spatial distribution of electron densities in the HOMO and LUMO. The red and green regions represent the positive and negative phases of the molecular orbitals, respectively. The HOMO is primarily localized over the aromatic conjugated system, suggesting that these sites act as potential electron donors. Conversely, the LUMO is mainly delocalized over the central quinonoid structure, highlighting the regions most favorable for electron acceptance.

The computed energies of the FMOs and related molecular properties are summarized in Table 4. The HOMO and LUMO energies were calculated as –5.49 eV and –2.34 eV, respectively, resulting in an energy gap of 2.85 eV. This relatively moderate gap indicates that DAAQ possesses both good stability and favorable polarizability, making it potentially useful in optoelectronic and photonic applications. The obtained energy gap is in close agreement with the band gap values reported for similar bioactive molecules, suggesting that DAAQ may share comparable chemical and biological properties.

Based on Koopmans's theorem, further chemical descriptors were derived. The ionization energy (I) was found to be 5.49 eV, while the electron affinity (A) was 2.34 eV. From these values, the global hardness (η) and softness (S) were calculated as 1.45 eV and 0.69 eV^{-1}, respectively. The chemical potential (μ) was –3.91 eV, and the electrophilicity index (Ψ) was 5.27 eV, indicating a moderate tendency of DAAQ to accept electrons.

Thus, the FMO analysis confirms that the DAAQ molecule has a stable structure with promising reactivity features. The distribution of electron density in HOMO and LUMO orbitals demonstrates the potential for strong electronic transitions, supporting the UV–Vis spectral findings. These results underline the importance of FMOs in understanding the molecular reactivity and photophysical behavior of DAAQ.

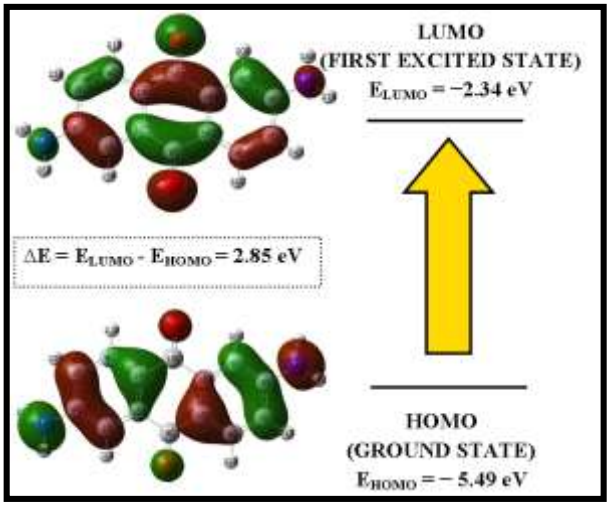

Fig.5. FMOs of DAAQ molecule

Table 4. The calculated FMOs and related molecular properties of the DAAQ molecule.

Molecular properties	Energy (eV)	Molecular properties	Energy (eV)
Energy (a.u.)	-799.29 a.u.	Electron Affinity (A)	2.34
E_{HOMO} (eV)	-5.49	Global hardness (η)	1.45
E_{LUMO} (eV)	-2.34	Chemical potential (μ)	-3.91
Energy gap (eV)	2.85	Electrophilicity index (Ψ)	5.27
Ionization energy (I)	5.49	Softness (S)	0.69

REDVET - Revista electrónica de Veterinaria - ISSN 1695-7504
Vol 25, No. 2 (2024)
http://www.veterinaria.org
Article Received: 16 September 2024 Revised: 18 October 2024
Accepted: 09 December 2024

3.5 Mulliken atomic charge distribution analysis

Mulliken population analysis is a powerful tool for examining the electron density distribution within molecules, as it significantly influences their dipole moment, polarizability, reactivity, and intermolecular interactions [26]. The Mulliken atomic charge distribution for the DAAQ molecule was computed using the DFT/B3LYP method with the cc-pVTZ basis set, and the results are depicted in Fig. 6. The analysis shows that the carbon atoms C2 and C6 carry the highest positive charges (+0.343). This is attributed to their direct bonding with the electronegative nitrogen atoms N13 and N14, which exhibit large negative charges (–0.811). The strong electron-withdrawing nature of nitrogen leads to significant electron density delocalization from adjacent carbons, thereby polarizing the electronic structure of DAAQ.

The oxygen atoms O11 and O12 are also highly electronegative, with charges of –0.437, further contributing to the overall negative charge concentration in the quinonoid framework. These atoms are likely to serve as active centers for hydrogen bonding or interactions with electrophiles. Other aromatic carbons (C1, C3–C5, C7, and C8) display moderately negative charges in the range of –0.141 to –0.188, reflecting the delocalization of π-electrons within the aromatic ring system. In contrast, carbons C9 and C10 are more positively charged (+0.176), indicating localized electron deficiency in those positions. The terminal carbons C15–C18 exhibit small but consistent positive charges (+0.060), suggesting a balanced distribution of charge density across the molecular periphery.

Hydrogen atoms display predominantly positive charges, as expected. Most hydrogens lie between +0.123 e and +0.167, while the terminal hydrogens H25–H28 show markedly higher positive charges (+0.321 to +0.326). This highlights their attachment to carbons already electron-deficient due to neighboring electronegative atoms, making these hydrogens potential sites for intermolecular interactions. Thus, the Mulliken charge distribution analysis confirms that nitrogen and oxygen atoms dominate the electron-withdrawing characteristics, while carbons adjacent to these atoms exhibit significant positive polarity. The extensive charge delocalization across the quinonoid and aromatic framework enhances the electronic communication within the molecule. This delocalization not only stabilizes the DAAQ structure but also contributes to its bioactivity and observed optical properties.

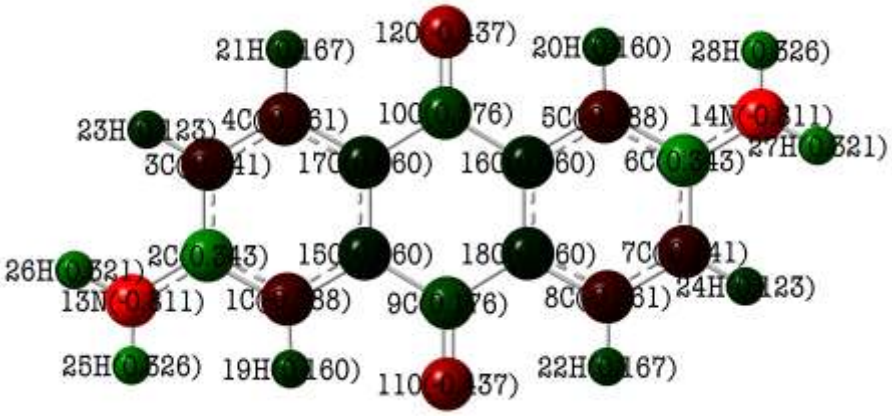

Fig. 6. Mulliken atomic charge distribution of DAAQ molecule

3.6 Molecular Electrostatic Potential (MEP) Surface Analysis

The molecular electrostatic potential (MEP) surface is a valuable tool to visualize the charge distribution and electrostatic interactions within a molecule [27]. It provides insights into the electrophilic and nucleophilic reactive sites by mapping the electron density onto an isosurface. The MEP surface of the DAAQ molecule, calculated at the B3LYP/cc-pVTZ level of theory, is illustrated in Fig. 7. In the MEP surface, red regions correspond to areas of negative electrostatic potential, typically associated with electron-rich centers that can act as nucleophilic sites. Conversely, blue regions indicate positive electrostatic potential, representing electron-deficient sites that are prone to electrophilic attack. Green regions correspond to regions of near-zero potential, indicating areas of neutral charge distribution.

For the DAAQ molecule, the most intense red regions are located around the oxygen atoms (O11 and O12) reflecting their strong electronegativity and tendency to attract electrophiles. This finding is consistent with the Mulliken charge distribution, where these atoms showed the highest negative charges. On the other hand, the positive potential (blue) regions are concentrated near the hydrogen atoms, particularly H25–H28, which are attached to electron-deficient carbons. These hydrogens are therefore the most favorable sites for nucleophilic interactions. The moderate distribution of green regions over the aromatic carbons highlights the delocalization of π-electrons across the conjugated framework, which contributes to the molecule's overall electronic stability and polarizability. The observed MEP features suggest that the DAAQ molecule possesses significant electronic asymmetry, with well-defined nucleophilic and electrophilic

REDVET - Revista electrónica de Veterinaria - ISSN 1695-7504
Vol 25, No. 2 (2024)
http://www.veterinaria.org
Article Received: 16 September 2024 Revised: 18 October 2024
Accepted: 09 December 2024

regions. This polarity enhances the molecule's potential for intermolecular interactions such as hydrogen bonding, charge transfer, and binding with biological targets, thereby influencing its chemical reactivity and bioactivity.

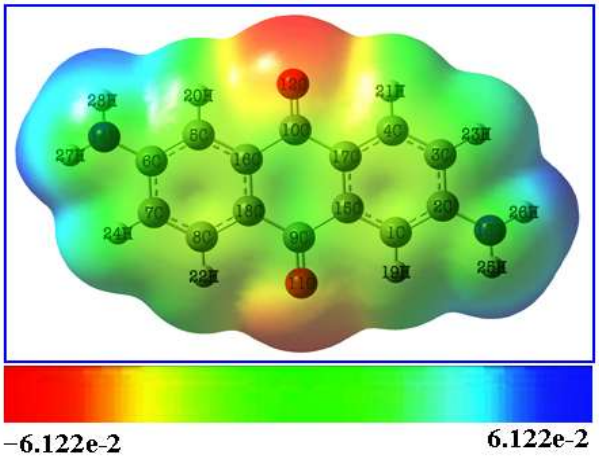

Fig. 7. MEP surface of DAAQ molecule.

3.7 Molecular docking Analysis

Molecular docking serves as a pivotal tool in drug discovery, enabling the prediction of binding affinities and interaction profiles between ligands and target proteins, thereby providing valuable insights into their therapeutic potential [28]. In this work, docking simulations were carried out using the DAAQ molecule as the ligand against two cancer-associated proteins: Dipeptidyl Peptidase-4 (DPP-4, PDB ID: 2ONC), a target relevant to lung cancer, and p38α Mitogen-activated Protein Kinase 14 (p38α MAPK, PDB ID: 3FMK), associated with cervical cancer. The docking analysis yielded the lowest-energy binding conformations, illustrated in Fig. 8. The DAAQ molecule demonstrated a stronger binding affinity toward DPP-4, with a docking score of −7.25 kcal/mol, compared to −6.10 kcal/mol for p38α MAPK. The lower binding energy in the case of DPP-4 highlights a more stable and favorable ligand-protein interaction, suggesting that DAAQ may possess superior inhibitory potential against lung cancer compared to cervical cancer.

A detailed inspection of the binding interactions revealed the presence of multiple hydrogen bonds that play a critical role in stabilizing the complexes. For DPP-4 (PDB ID: 2ONC), the DAAQ molecule established hydrogen bonds with VAL 558 (3.5 Å) and PRO 510 (3.5 Å), reinforcing the overall stability of the ligand-protein complex. Conversely, in p38α MAPK (PDB ID: 3FMK), the DAAQ molecule formed hydrogen bonds with ARG 94 (2.5 Å), THR 91 (2.1 Å), and VAL 89 (2.3 Å). Although multiple interactions were observed, the binding affinity remained weaker than that with DPP-4, suggesting a comparatively less stable interaction. The stronger binding affinity and favorable hydrogen bonding pattern observed with DPP-4 correlate with the in vitro cytotoxicity results, where DAAQ exhibited a relatively low IC_{50} value of 3.95 µg/ml against A549 lung cancer cells, indicating potent inhibition. In contrast, its higher IC_{50} value of 12.87 µg/ml against HeLa cervical cancer cells aligns with the weaker interaction observed with p38α MAPK.

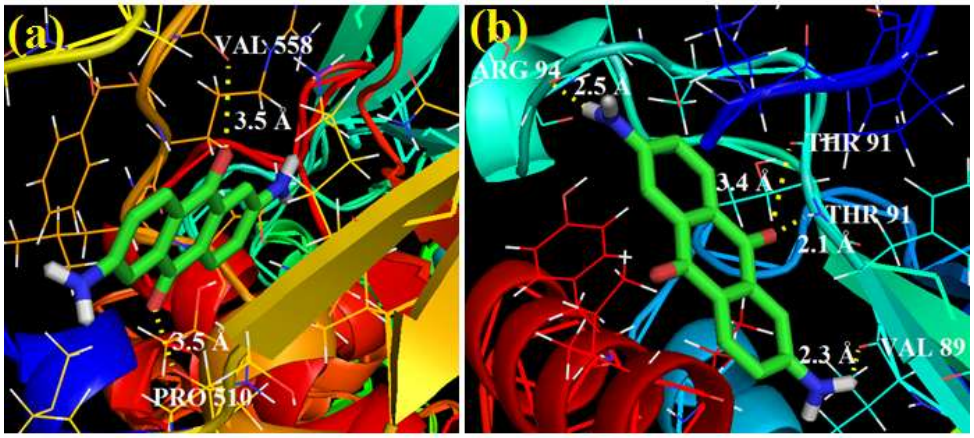

Fig. 8. The lowest energy docked poses of the DAAQ ligand with targeted proteins including (a) Dipeptidyl Peptidase-4 (DPP-4) [PDB ID: 2ONC] and (b) p38α Mitogen-activated protein kinase 14 (p38α MAPK) [PDB ID: 3FMK]

REDVET - Revista electrónica de Veterinaria - ISSN 1695-7504
Vol 25, No. 2 (2024)
http://www.veterinaria.org
Article Received: 16 September 2024 Revised: 18 October 2024
Accepted: 09 December 2024

3.8 In Vitro Cytotoxicity Anticancer Studies

3.8.1 MTT Assay

The cytotoxic activity of the DAAQ molecule was evaluated against A549 (lung cancer) and HeLa (cervical cancer) cell lines using the MTT assay. Cells were exposed to varying concentrations of DAAQ (0–360 µg/mL) for 24 hours, and the percentage of viable cells was quantified to assess its anticancer efficacy. The results, shown in Fig. 9 for A549 cells and Fig. 10 for HeLa cells, clearly demonstrate a dose-dependent decline in cell viability, confirming the concentration-dependent cytotoxic nature of DAAQ.

In the case of A549 lung cancer cells, a significant reduction in viability was observed even at relatively lower concentrations. A noticeable decrease began around 60 µg/mL, and by 150 µg/mL, a sharp decline in cell survival was evident. At 300 µg/mL, the majority of A549 cells lost viability, and at the highest tested concentration (360 µg/mL), cell viability was reduced to below 30%. The calculated IC_{50} value was 3.95 µg/mL, indicating potent cytotoxic activity of DAAQ against A549 cells. This strong inhibitory effect correlates with the molecular docking results, where DAAQ exhibited higher binding affinity (−7.25 kcal/mol) toward the DPP-4 protein (PDB ID: 2ONC), further supporting its selective efficacy against lung cancer.

For HeLa cervical cancer cells, cytotoxic effects were less pronounced at lower concentrations (50–150 µg/mL), with only a mild reduction in cell viability. A more distinct decline in survival was evident at 225–300 µg/mL, and at 360 µg/mL, cell viability dropped below 20%. The determined IC_{50} value was 12.87 µg/mL, reflecting moderate cytotoxic potential compared to A549 cells. These findings are consistent with the docking outcomes, where DAAQ displayed relatively weaker binding affinity (−6.10 kcal/mol) with p38α MAPK (PDB ID: 3FMK), suggesting a lower inhibitory effect against cervical cancer.

The greater sensitivity of A549 cells to DAAQ may be attributed to the stronger hydrogen bonding and hydrophobic interactions with DPP-4, which play critical roles in regulating cancer cell proliferation and survival. In contrast, the weaker binding interactions observed with p38α MAPK in HeLa cells align with the higher IC_{50} value, highlighting reduced susceptibility.Morphological observations further confirmed these findings, where both A549 and HeLa cells displayed hallmarks of apoptotic cell death after DAAQ treatment, including cell shrinkage, detachment, membrane rupture, and nuclear condensation (Fig. 11).

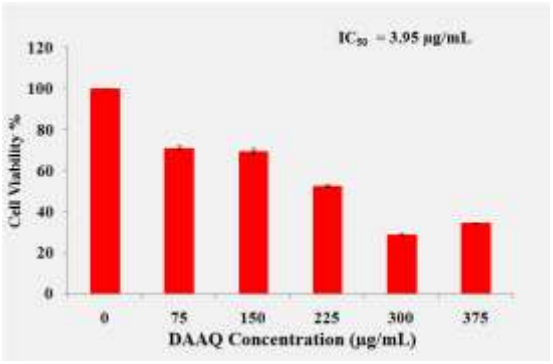

Fig. 9. MTT assay measurement on different percentages of cell viability in A549 Lung cancer cell lines against varied concentrations of DAAQ compound.

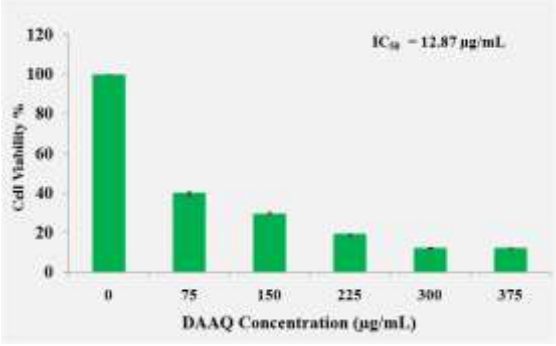

Fig.10. MTT assay measurement on different percentages of cell viability in HeLa cervical cancer cell lines against varied concentrations of DAAQ compound.

REDVET - Revista electrónica de Veterinaria - ISSN 1695-7504
Vol 25, No. 2 (2024)
http://www.veterinaria.org
Article Received: 16 September 2024 Revised: 18 October 2024
Accepted: 09 December 2024

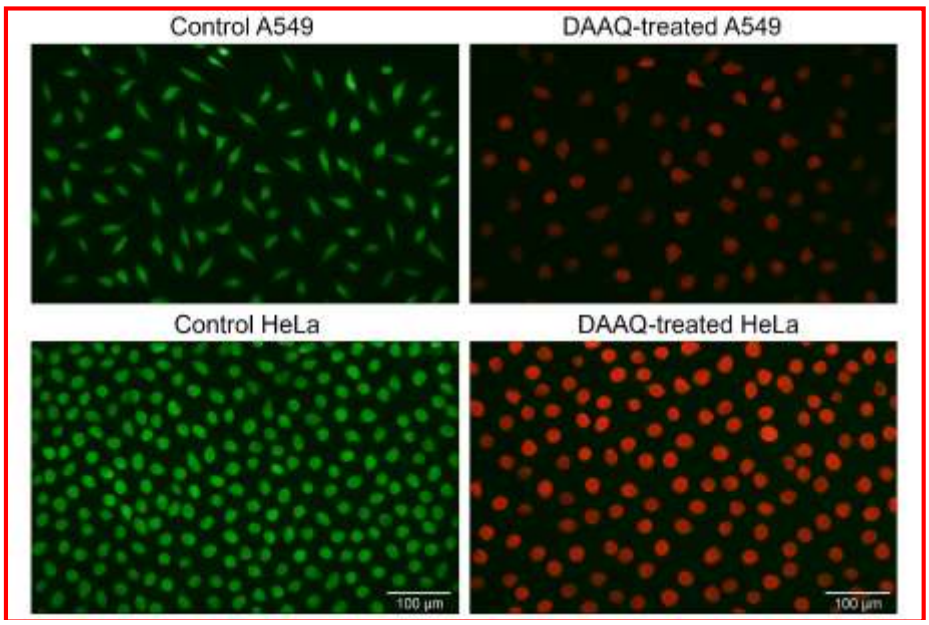

Fig. 11. Morphological profile of the A549 Lung cancer cells (a) control and (b) after treated with DAAQ compound for 24 hours and the morphological profile of the HeLa Cervical cancer cells (c) control and (d) after treated with DAAQ compound for 24 hours.

4. Conclusion

In this work, the structural, spectroscopic, and biological properties ossf 2,6-Diaminoanthraquinone (DAAQ) were systematically investigated through a combination of DFT calculations, FT-IR/FT-Raman spectroscopy, and in vitro cytotoxicity assays. Geometry optimization at the B3LYP/cc-pVTZ level confirmed that DAAQ adopts a nearly planar, fully conjugated anthraquinone framework with effective π-electron delocalization between the electron-donating amino groups and the electron-withdrawing carbonyl units. Bond lengths, bond angles, and dihedral angles corroborated the resonance-assisted conjugation of the $–NH_2$ substituents with the aromatic skeleton A detailed vibrational analysis of 78 normal modes, supported by PED assignments and scaling factors, provided reliable characterization of functional group vibrations. Theoretical predictions were in excellent agreement with experimental FT-IR and FT-Raman spectra. Furthermore, cytotoxicity assays against A549 lung cancer cells and HeLa cervical cancer cells revealed that DAAQ exhibits significant inhibitory activity, consistent with its π-conjugated anthraquinone core and functional substituents known to interact with biomolecular targets. Morphological changes in treated cells confirmed apoptosis-like cell death, underscoring the therapeutic potential of DAAQ.

Acknowledgements

The authors extend their sincere gratitude to the college management for their support and for granting permission to perform this research. Dr. R. Premkumar also extends his gratitude to the management of Nadar Mahajana Sangam S. Vellaichamy Nadar College for granting access to the Advanced Materials Research Centre in the PG and Research Department of Physics, which was instrumental in this study. Additionally, heartfelt thanks are extended to SAIF at IIT-Madras for their assistance in recording the FT-IR, FT-Raman, and UV-Vis spectra of the sample.

References

[1] Siegel RL, Miller KD, Wagle NS, Jemal A (2023) Cancer statistics, CA Cancer J Clin.73(1):17–48.
[2] Herbst RS, Morgensztern D, Boshoff C (2018) The biology and management of non-small cell lung cancer, Nature 553:446–454.
[3] Arbyn M, Weiderpass E, Bruni L, de Sanjosé S, Saraiya M, Ferlay J, Bray F (2020) Estimates of incidence and mortality of cervical cancer in 2018: a worldwide analysis. Lancet Glob Health 8(2)\:e191–e203.
[4] Crosbie EJ, Einstein MH, Franceschi S, Kitchener HC (2013) Human papillomavirus and cervical cancer. Lancet 382(9895):889–899.
[5] Duval J, Pecher V, Poujol M, Lesellier E (2016) Research advances for the extraction, analysis and uses of anthraquinones: A review. Ind Crops Prod. 94:812–833.
[6] Huang Q, Lu G, Shen HM, Chung MCM, Ong CN (2007) Anti-cancer properties of anthraquinones from rhubarb. Med Res Rev. 27:609–630.
[7] Schripsema J, Dagnino D (1996) Elucidation of the substitution pattern of 9,10-anthraquinones through the chemical shifts of peri-hydroxyl protons. Phytochemistry 42:177–184.

[8] Andersen DO, Weber ND, Wood SG, Hughes BG, Murray BK, North JA (1991) In vitro virucidal activity of selected anthraquinones and anthraquinone derivatives. Antiviral Res. 16:185–196.
[9] Valarmathi T, Premkumar R, Benial AMF (2020) Spectroscopic and molecular docking studies on 1-hydroxyanthraquinone: A potent ovarian cancer drug. J Mol Struct. 1213:128163.
[10] Geetha R, Meera MR, Vijayakumar C, Premkumar R, Benial AMF (2023) Synthesis, spectroscopic characterization, molecular docking and in vitro cytotoxicity investigations on 8-amino-6-methoxy quinolinium picrate: A novel breast cancer drug. J Biomol Struct Dyn. 41(5):1753–1766.
[11] Jamróz M.H. (2004) Vibrational Energy Distribution Analysis VEDA 4: Program for Vibrational Mode Analysis, Warsaw, Poland.
[12] Morris GM, Huey R, Lindstrom W, Sanner MF, Belew RK, Goodsell DS, Olson AJ (2009) AutoDock4 and AutoDockTools4: Automated docking with selective receptor flexibility. J Comput Chem 30(16):2785–2791.
[13] Frisch G W, Trucks H B, Schlegel, et al. Gaussian 09, Revision C.02, Gaussian Inc., Wallingford CT, 2009.
[14] Jamróz M H (2004) Vibrational Energy Distribution Analysis VEDA 4: Program for Vibrational Mode Analysis, Warsaw, Poland.
[15] Dennington R, Keith T, Millam J (2009) GaussView, Version 5.0, Semichem Inc., Shawnee Mission, KS.
[16] Morris G M, Huey R, Lindstrom W, Sanner M F, Belew R K, Goodsell D S, Olson A J (2009) AutoDock4 and AutoDockTools4: Automated docking with selective receptor flexibility. J Comput Chem 30(16):2785–2791.
[17] Wesley U V, Tiwari S, Houghton A N (2004) Role for dipeptidyl peptidase IV in tumor suppression of human non-small cell lung carcinoma cells. Int J Cancer 109(6):855–866.
[18] Bulavin D V, Fornace A J (2004) p38 MAP kinase's emerging role as a tumor suppressor. Adv Cancer Res 92:95–118.
[19] Khan, M. S.; Kumar, S.; Choudhury, A. R. (2017) Structural, electronic, and vibrational study of anthraquinone derivatives: A DFT approach. J. Mol. Struct. 1134, 469–478.
[20] Ghosh, S.; Jana, P. K.; Mukherjee, S. (2016) Theoretical studies on substituted anthraquinones: Structure, conjugation, and electronic effects. Comput. Theor. Chem. 2016, 1094, 1–9.
[21] Varsányi, G. Assignments for Vibrational Spectra of Seven Hundred Benzene Derivatives; Academic Press: New York, 1974.
[22] Hollas, J. M. Modern Spectroscopy, 4th Ed.; Wiley: Chichester, 2004.
[23] Pretsch, E.; Bühlmann, P.; Badertscher, M.Structure Determination of Organic Compounds: Tables of Spectral Data, 4th Ed.; Springer: Berlin, 2009
[24] T. Valarmathi, E. James Jebaseelan Samuel, R. Premkumar, A. Milton Franklin Benial (2023) Spectroscopic Characterization, Quantum Chemical and Molecular Docking Studies on 1-Chloroanthraquinone: A Novel Oral Squamous Cell Carcinoma Drug, Polycyclic Aromatic Compounds, DOI: 10.1080/10406638.2023.2209249 (2023)
[25]K. Langeswaran, Saad AlGarni, M.Muthuramamoorthy, P. Saravanan, R. Premkumar*, R. Sangeetha (2025) 4-Fluorochalcone as a novel therapeutic agent for cervical cancer: An in-depth spectroscopic and computational study, Journal of Molecular Structure 1326 (2025) 141130.
[26] R. Geetha, M.R. Meera, C. Vijayakumar, R. Premkumar*, R. Govindharaju (2024) Synthesis, spectroscopic characterization, biological evaluation studies on 6-methoxy-8-nitroquinolinium picrate: A potent lung cancer drug, Journal of Molecular Structure 1317, 139029.
[27] Ganesan Venkatesh, Palanisamy Vennila, Savas Kaya, Samia Ben Ahmed, Paramasivam Sumathi, Vadivel Siva, Premkumar Rajendran, Chennapan Kamal (2024) Synthesis and Spectroscopic Characterization of Schiff Base Metal Complexes, Biological Activity, and Molecular Docking Studies, ACS Omega, DOI: 10.1021/acsomega.3c08526 (2024).
[28] V. Meenakumari, J. Mangaiyarkkarasi, R. Premkumar, R. Mohamed Asath, T. Thenmozhi, A. Milton Franklin Benial (2024) Spectroscopic Characterization, Quantum Chemical and Molecular Docking Investigations on Methyl Indole-3-Carboxylate: A Potent Cervical Cancer Drug, Journal of Molecular Structure, 1305(17) (2024) 137711.